Title

Combined Experimental and Theoretical Investigation of Heating Rate on Growth of Iron Oxide Nanoparticles

Authors

Dehsari, Hamed Sharifi
Heidari, Maziar
Ribeiro, Anielen Halda
et al.

Combined Experimental and Theoretical Investigation of Heating Rate on Growth of Iron Oxide Nanoparticles

Hamed Sharifi Dehsari,[†] Maziar Heidari,[†] Anielen Halda Ribeiro,[†] Wolfgang Tremel,[‡] Gerhard Jakob,[§] Davide Donadio,[‖] Raffaello Potestio,*[,†] and Kamal Asadi*[,†]

[†]Max Planck Institute for Polymer Research, Ackermannweg 10, 55128 Mainz, Germany

[‡]Institute of Inorganic Chemistry and Analytical Chemistry, Johannes Gutenberg University, Duesbergweg 10, 55099 Mainz, Germany

[§]Institute of Physics, Johannes Gutenberg University, Staudinger Weg 7, 55099 Mainz, Germany

[‖]Department of Chemistry, University of California Davis, One Shields Avenue, Davis, California 95616, United States

ⓢ *Supporting Information*

ABSTRACT: Thermal decomposition is a promising route for the synthesis of highly monodisperse magnetite nanoparticles. However, the apparent simplicity of the synthesis is counterbalanced by the complex interplay of the reagents with the reaction variables that determine the final particle size and dispersity. Here, we present a combined experimental and theoretical study on the influence of the heating rate on crystal growth, size, and monodispersity of iron oxide nanoparticles. We synthesized monodisperse nanoparticles with sizes varying from 6.3 to 27 nm simply by controlling the heating rate of the reaction. The nanoparticles show size-dependent superparamagnetic behavior. Using numerical calculations based on the classical nucleation theory and growth model, we identified the relative time scales associated with the heating rate and precursor-to-monomer (growth species) conversion rate as a decisive factor influencing the final size and dispersity of the nanoparticles.
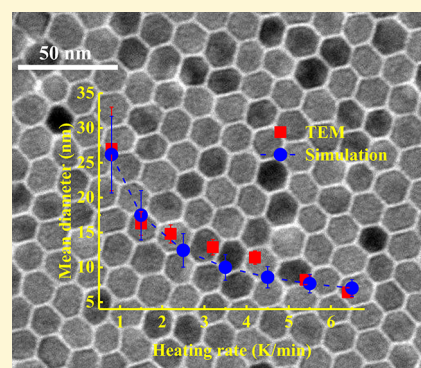
INTRODUCTION

Iron oxide nanoparticles (NPs) are among the most promising candidates for data storage,[1,2] catalysis,[3] and (bio)medical imaging,[4−6] owing to their magnetic properties,[7] biocompatibility,[5] and environmental friendliness.[8,9] The synthesis of monodisperse NPs with well-defined sizes is a key factor for applications, as the size strongly influences the NPs' magnetic properties.[10,11] Iron oxide NPs have been made using different methods.[12−16] The synthesis via thermal decomposition, where the precursor solution prepared at low temperature is heated up to a high temperature, is an established route to make size-controlled NPs.[17−20] In a typical reaction, an organometallic precursor is decomposed at high temperature in a solvent with a high boiling point, and subsequently the NP is formed after supersaturation is reached. Organic ligands, such as oleic acids and oleylamine, are typical surfactants that serve as stabilizers during the reaction.[21,20]

In a typical thermal decomposition reaction, the precursors, either reagents or the secondary complexes, undergo an increased thermodynamic driving force to form "monomers". Reaction of monomers with each other leads to formation of nuclei. The nucleation of nascent NPs is triggered by the heating process. Upon continued heating during reflux time, the initial nuclei grow into mature NPs. Thermal decomposition endows specific subtleties due to the complex interplay between reaction variables, such as concentrations of precursors,[22] solvent,[23] and surfactants,[24] as well as solvent boiling point,[25,18,20] reaction time,[26,27] and precursor-to-surfactant ratio,[25,22,24] all of which drastically influence the final size and the respective size distribution of the NP. In a typical thermal decomposition synthesis, the heating rate is a crucial factor because it impacts nucleation through the monomer concentration. Tuning the heating rate is therefore a rational way to modulate the nucleation process and consequently to tune the final size and concentration of the NPs.[28,29]

The underlying phenomenology of the particle formation mechanism can be usually understood within the context of classical nucleation and growth theory and within a model proposed by LaMer.[30] The nucleation and growth of NPs is described by a set of coupled time-dependent equations that govern the dynamics of monomer concentration, nucleation rate, and particle size distribution.[31−33,28,34] A numerical treatment provides a powerful tool for a better understanding of the nucleation and growth processes of NPs at the molecular level and therefore provides information on how to design an effective synthesis. As a result, a more systematically controlled synthesis can be devised.
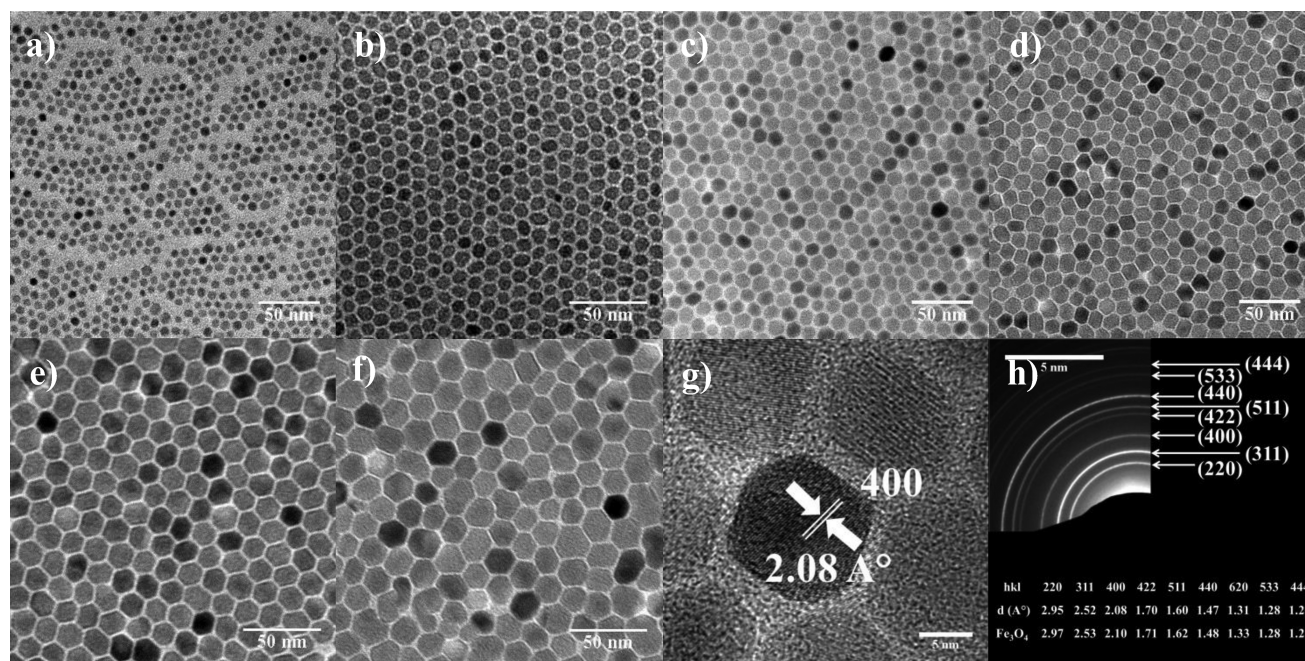
Figure 1. TEM images of (a) A_1, (b) A_2, (c) A_3, (d) A_4, (e) A_5, and (f) A_6 reactions. (g) HRTEM images of sample A_4 and (h) SAED pattern of the same A_4 sample and measured lattice spacings, d (Å), using the rings and standard atomic spacings for NPs following with their respective hkl indices.

In this work, we present a combined experimental and theoretical study on the size evolution of magnetic iron oxide NPs while varying only the heating rate during synthesis. NPs with controllable sizes from 6 to 27 nm were obtained with a narrow size distribution (typically below 10%). Crystallinity and the magnetic properties of the NP were investigated using different analytical techniques.

The NPs are crystallized in inverse spinel structure with a high degree of crystallinity. The particles are superparamagnetic and show an increase in saturation magnetization with increasing size, with a disorder magnetic shell of less than 0.5 nm. To gain further insight concerning the NP formation, we numerically simulated the nucleation and growth process at different heating rates. The model employed describes the time-dependent evolution of the NP size distribution (among other observables), and it enabled us to perform a quantitative analysis of the specific system parameters, which mainly influence the experimental outputs. The numerical simulations reproduce the observed experimental trends with reasonable accuracy and allowed us to pinpoint the relative time scales associated with the heating rate and precursor-to-monomer conversion rate as the decisive factor influencing the NP final size and dispersity in synthesis by heat-up processes.

■ EXPERIMENTAL SECTION

Iron(III) acetylacetonate (97%), oleylamine (OAM, >70%), benzyl ether (BE, technical grade 98%), oleic acid (OAC, technical grade, 90%), hexane, ethanol, and acetone were purchased from Sigma-Aldrich. Hexadecandiol (99%) was purchased from TCI. All chemicals were used as received. For synthesis of the NPs, 2.0 mmol of iron acetylacetonate, 10 mmol of hexadecandiol, 6 mmol of oleylamine, and 6 mmol of oleic acid were mixed in 20 mL of benzyl ether in a three-necked round-bottom flask under a gentle flow of N_2. The mixture was magnetically stirred and degassed under vacuum (0.1−0.2 mbar) at 383 K (110 °C) for 60 min. Under N_2 blanketing, the temperature was then raised to 453 K (180 °C), with a heating rate (HR) of about 6.5 K/min. The solution was kept at 453 K for 2 h to ensure full

decomposition of the precursor. Subsequently, the solution was heated to a reflux temperature of almost 567 K (~294 °C) at a constant heating rate. Different syntheses were performed in which the heating rates were systematically varied from 6.4 (A_1) to 5.4 (A_2), 4.2 (A_3), 3.2 (A_4), 2.2(A_5), 1.5 (A_6), and 0.8 K/min (A_7), where A_i represents the synthesis batch. The reaction was kept at the reflux temperature for 1 h. Figure S1 in the Supporting Information (SI) schematically summarizes the reaction conditions. The resultant black solution was cooled down to room temperature under N_2 blanketing. After precipitation of the product by adding 40 mL of ethanol/acetone, a mild centrifugation (6000 rpm for 8 min) was applied to collect the purified product. The NPs formed a stable dispersion in toluene/hexane after further purification by dispersion in hexane and precipitation by ethanol.

The NPs were characterized by transmission electron microscopy (TEM) and high-resolution TEM (HRTEM), with an accelerating voltage of 120 kV on a JEOL JEM1400 instrument, and 200 kV on FEI Tecnai F20 200 kV instrument, respectively. The size distribution of NPs was calculated from the size measurements of more than 2000 NPs. Samples were prepared using the self-assembly method at the water−air interface.[35] The X-ray diffraction (XRD) was performed at room temperature with a monochromatic copper radiation source Cu Kα (λ = 1.5406 Å) in the 15−65° (2θ) range with a scan step of 0.03°. The mean size and lattice parameter of the crystal domains were calculated from XRD pattern by using Scherrer and Bragg equations,[36−38] respectively. Details of XRD analysis are presented in the SI. Infrared spectra were recorded between 4000 and 400 cm^{-1} with a Fourier transform infrared (FTIR) spectrometer. The NPs were gently ground and diluted with KBr and compressed into a pellet. Thermogravimetric measurements were performed on dried powder samples from 20 to 800 °C at 10 °C/min under N_2. Magnetization measurements of powder samples were performed using a quantum design SQUID magnetometer. Hysteresis loops $M(H)$ were measured at room temperature and 2 K. Zero-field-cooling (ZFC) and field-cooling (FC) magnetization curves were performed in the temperature range 5−300 K to determine blocking temperature, T_B, and magnetic anisotropy constant, K.

■ RESULTS AND DISCUSSION

Experimental Study of Nanoparticle Size Evolution.
Because of monodispersity and shape regularity, the NPs have a strong tendency to self-assemble as shown in the large-view TEM images of Figure S2 in the SI. Figure 1a−f shows that the heating rate has a dramatic effect on the NP size. The particle shape evolves with size and varies from pseudospherical for A_1 and A_2 to faceted polyhedra for A_3−A_6. The average particle diameter, D_{TEM}, and the standard deviations, σ_{TEM}'s, were derived from size distribution histograms obtained from the TEM images. The size distribution histograms of the NPs are given in Figure S3. As the heating rate increased from 0.8 to 6.4 K/min, the size of the NP decreased from 27 to 6.3 nm. The polydispersity index for all NP batches was typically around 10%. We note that the heating rate (first heating rate) applied to reach the decomposition temperature of 453 K has no influence on the final NP size. To unambiguously rule out the effect of the first heating rate, we performed synthesis with three different rates of 5, 6.5, and 8 K/min. The mean NP size did not show variation with a different first heating rate, as shown in Figure S4 and in agreement with previous literature reports.[39]

Further structural information was obtained from high-resolution TEM, HRTEM, and selected area electron diffraction, SAED. A representative HRTEM image of a single NP with a diameter of 13.0 nm (A_4) is shown in Figure 1g. HRTEM images of other samples are given in Figure S5 in the SI. The HRTEM images show the presence of a high-quality single-crystalline phase in the A_4 (and likewise for other) NPs. The measured interplanar distances from adjacent lattice fringes are consistent with known values of face centered cubic (fcc) Fe_3O_4[25,37,20] (Figure 1g). A characteristic SAED pattern is shown in Figure 1h for sample A_4. The measured d_{hkl} values for A_4 NPs are listed in the inset of Figure 1h and match well with the reported values for bulk magnetite (Fe_3O_4).[25,20]

The crystal size and structure of the NPs were further investigated with XRD. The diffraction patterns and the intensities, as shown in Figure 2, could be indexed to an inverse spinel structure. Interplanar distance d_{hkl} (Å) (311) values for all NPs were calculated, as shown in Figure S6 (SI) and compared with those of stoichiometric magnetite Fe_3O_4 (8.396 Å; 0.8396 nm, JCPDS 19-629) and maghemite γ-Fe_2O_3 (8.346 Å; 0.8346 nm, JCPDS 39-1346) phases.[25,40,41] The value of the lattice constant increases with increasing particle size, and changes from maghemite for the smallest particles A_1 to stoichiometric magnetite for the larger particles. The crystalline sizes were also obtained from (311) reflection, as discussed in the SI. A summary of the NP crystal size evolution with heating rate is given in Figure 3. The particle crystal size for A_1–A_6 is consistent with the statistical analysis of the TEM images, implicitly indicating single crystallinity of the individual particles. We note that the ligand shell around the NPs is predominantly oleate as determined from FTIR spectra of the NPs (Figure S7). Surfactant coverage was determined with TGA and DTG (Figure S8); the weight loss systematically changes from 28.2% for 6.3 nm to 7.2% for 27 nm. Further information for FTIR and TGA can be found in the SI. Furthermore, using TGA data and subtraction of the mass of the organic ligand, the mass reaction yield of the pure inorganic nanoparticle for three different heating rates of 2.2, 3.2, and 5.4 K/min amounted to 75.5%, 80.5%, and 81%, respectively, in good agreement with reported literature values.[42]
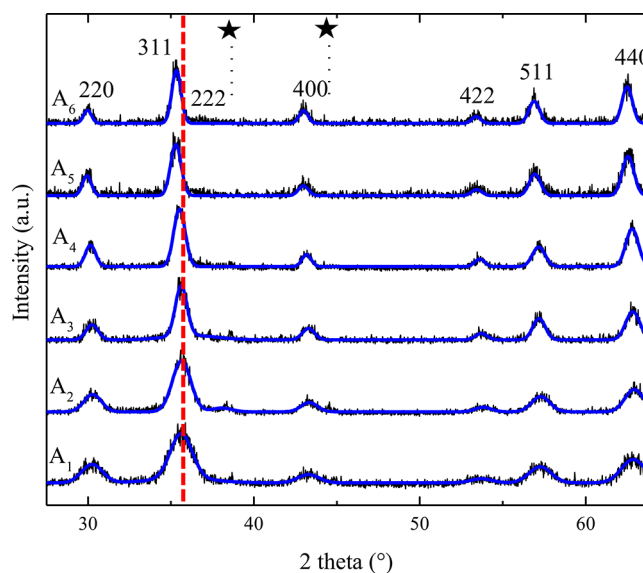

Figure 2. XRD diffractograms of all nanoparticles (black) and their corresponding modeling (blue). Positions of the Bragg reflections of the sample holder are indicated by stars. Red dashed line is for highlighting the peak position in (311).
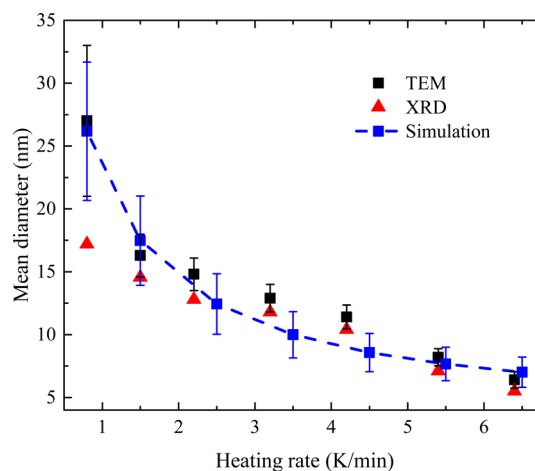

Figure 3. Mean diameter of NPs as a function of heating rate obtained via TEM and XRD. The simulated NP size is obtained with an activation energy of E_A = 70 kJ/mol. The error bars represent size dispersion at fwhm of the particle size histograms.

Modeling of Nanoparticle Nucleation and Growth. To gain insight on NPs' nucleation and growth process at the molecular level, we set up a numerical model based on classical nucleation theory.[31−33,28] The model relies on a rate equation that accounts for population balance,[31,43−47,28,29,48] which describes the dynamics of the precursor-to-monomer conversion:

$$\frac{d[P]}{dt} = -\frac{d[C]}{dt} = -Ae^{-E_A/RT}[P] \qquad (1)$$

where [P] and [C] are the concentrations of precursors and monomers, respectively, E_A is the precursor-to-monomer activation energy, R is the gas constant, T is the system temperature, and A is a constant prefactor. The model is based on the kinetics of a population of Fe_3O_4 monomers. For the sake of simplicity, the surfactant is ignored. The population of monomers, and therefore supersaturation, defined as S = [C]/

$[C]_\infty$, increases upon heating. Formation of the nuclei is then thermodynamically allowed by the reaction of monomers. For the nuclei larger than a critical radius, r_c, further reaction of the monomers decreases the Gibbs free energy leading to stable nuclei. The rate at which the nuclei are formed, the nucleation rate, is determined by monomer concentration, surface energy, critical radius, and temperature, $R_{nuc} = f([C], \gamma, r_c, T)$. The nucleated NPs grow further to larger sizes as the time lapses. The number of NPs of radius r at time t has a distribution, $N(r, t)$, the time evolution of which reads as

$$\frac{dN(r, t)}{dt} = \frac{\partial N(r, t)}{\partial t} + \frac{\partial [N(r, t)\, \Gamma(r, t)]}{\partial r} = R_{nuc}g(r)$$

(2)

where $\Gamma(r, t)$ is the instantaneous growth rate. The nucleation rate, R_{nuc}, is the source term which accounts for the possibility of nucleating new NPs at a given time modulated by the size-dependent distribution function, $g(r)$. When nucleation is terminated, $R_{nuc} = 0$. Equation 2 still describes the growth of NPs with time, based on $\Gamma(r, t)$. A full description of the model is given in the SI.

For investigation of the NP size evolution with heating rate, simulations were performed by mimicking the experimental conditions. The following parameters needed in the model, namely, molar mass (M_w), initial mass of the precursors (M_i), and reaction volume (V_{tot}), are known *a priori* from the experimental setups. It was assumed that at $t = 0$, there are no particles, i.e., $N(r, t = 0) = 0$. At $t = 0$, the temperature was set at $T_0 = 453$ K (180 °C), and linearly increased up to $T_f = 567$ K (294 °C) with different heating rates. The system is kept at reflux temperature T_f for 3600 s. The amount of the NPs at the end of the simulation ($t = t_f$), was calculated by summing the number of NPs of all sizes, i.e., $N_{tf} = \sum_r N(r, t_f)$. Unfixed parameters, such as precursor-to-monomer activation energy, E_A, were explored within the physical range reported for nanocrystal growth.[28] An optimal set of parameters was identified, so that the simulated results follow closely the experimental trend for the NP size evolution. A full description of the parameters and the protocols followed to determine them are given in the SI. Figure 3 shows that the numerically calculated mean NP diameter monotonically decreases as a function of increasing heating rate, in excellent agreement with the experiment.

The effect of the heating rate on the final NP size can be explained quantitatively. We investigated the relative conversion rates of the precursor-to-monomer process as well as the relative dynamics of the system supersaturation. Three different heating rates were selected, namely, 1.5, 3.5, and 6.5 K/min which represent slow, intermediate, and fast heating rates, respectively. Figure 4a shows the time evolution of supersaturation. For a slow heating rate of 1.5 K/min, the precursor is slowly converted into monomers, and supersaturation increases slowly in time. The change in the total number of NPs in time, dN/dt, is directly proportional to nucleation rate, see eq 2. It has to be emphasized that, for all heating rates, the nucleation rate at the beginning of the simulation is negligible which is a key feature of the heat-up reaction. As supersaturation increases, after an elapsed time, $t = 1600$ s, nucleation starts. Despite the initiation of nucleation process and monomer consumption, supersaturation does not drop, because monomers are being produced progressively faster as the temperature rises (see eq 1). Once nucleation is triggered, increase in the supersaturation is sustained for a
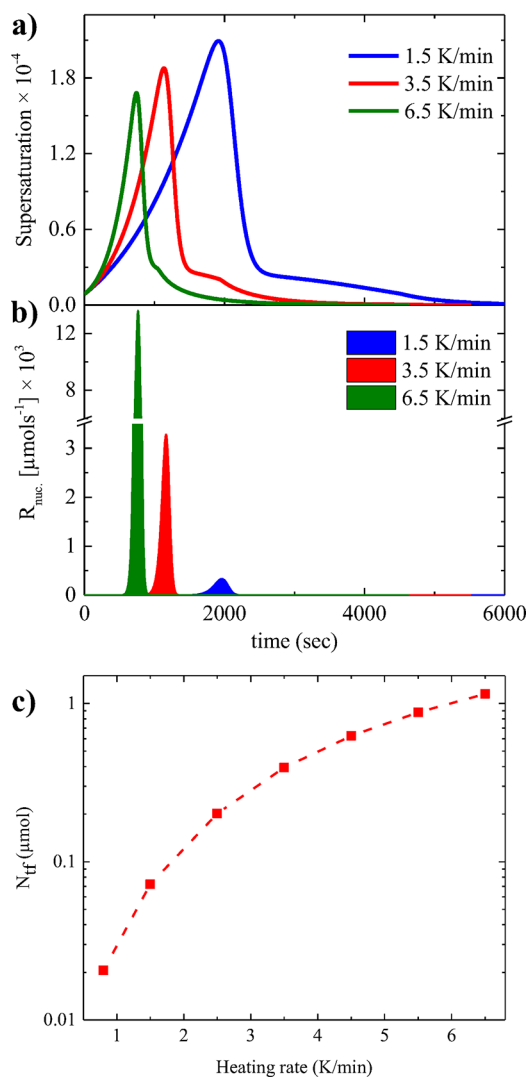

Figure 4. (a) Simulated supersaturation profiles of reactions at different heating rates along the simulation time. (b) Corresponding nucleation rate for the same heating rates used in part a. (c) Number of NPs at the end of simulation reflux time, 3600 s.

period of time until the system contains enough nuclei to result in a net decrease in the monomer concentration, which is associated with a substantial drop in supersaturation and subsequently quenching of the nucleation rate. Upon termination of the nucleation process, the remaining population of monomers then acts as a reservoir for the continued growth of the nascent nuclei. The remaining monomers are consumed at a rate faster than the precursor conversion rate until the monomer concentration becomes infinitesimally small and/or final simulation time is reached.

For higher heating rates the supersaturation shows a faster increase with time. The nucleation therefore occurs in earlier stages with relatively higher rates, as shown in Figure 4a,b. For fast heating rates, the release of monomer is much faster than the growth of the existing nuclei. The available monomers contribute almost solely to nucleation, resulting in a higher number of nascent nuclei. Upon termination of the nucleation, in contrast to the case of slow heating rate, the majority of the monomers are consumed. The remaining monomers must then be evenly distributed among a much larger number of nuclei, leading to significantly reduced final NP size.[49] The nucleation

process is much shorter (Figure 4b). A narrower nucleation window means that all NPs are formed and subsequently grow "almost" simultaneously. As a result, a higher heating rate would yield NPs with a narrower size distribution and better monodispersity. A good agreement between the calculated and experimentally observed polydispersity is obtained, as shown in Figure 3. We found out that activation energy E_A = 70 kJ/mol gives the best description of the experimental trend (as shall be discussed later). A natural consequence of higher heating rates is that N_{tf} at the end of simulation time increases as a function of increasing heating rate, as shown in Figure 4c. The evolution of the total number of NPs in the course of simulation time for three representative different heating rates is shown in Figure S9. Moreover, an approximate nanoparticle count, N, could be determined using the experimentally determined mean diameter obtained from TEM images, and is shown in Figure S10 for three different heating rates. The trend of increasing N with the heating rate is in good agreement with the simulation prediction. We note that, as result of postsynthesis purification steps, only an approximation of N can be given.

The evolution of mean diameter is predominantly determined during the heating stage. Shortly after the final temperature has been reached, the nanoparticle size and its deviation from the mean value approaches the final mean value and does not change further with increasing reflux time, as shown in Figure S11. Further syntheses were performed at a fixed heating rate of 3.2 K/min, and a different reflux time ranging from 0 to 360 min. The size of the resulting nanoparticles was fixed at 13.0 ± 1.2 nm, in accordance with the simulation data, and previous reports.[25,50]

The populations of the NPs for representative heating rates at different reaction times are shown in Figure 5. The critical radius, r_c, for each heating rate is marked with a symbol. At the beginning of the simulation, t = 1 s, the nascent nuclei appear around the critical radius. As the nucleation process continues, t = 100 s, the nascent nuclei grow to larger NPs and approximately reach the steady-state distribution around t = 2000 s. For the slowest heating rate, critical radius, r_c, does not change substantially with time. Therefore, the nuclei that are formed are stable and can grow further to NPs of larger sizes. For the fastest heating rate, however, r_c grows to larger values as the time lapses. Hence, early Ostwald ripening[34] takes place, and particles that are formed with $r < r_c$ dissolved into monomers favoring the growth of the larger particles.

The activation energy of the precursor-to-monomer conversion, E_A, is an influential parameter as it determines the relative time scales of the temperature rise and the monomer release rate. The sensitivity of the final NPs' diameter and standard deviation to the heating rates was therefore tested for very high and low activation energies, E_A = 90 kJ/mol and E_A = 5 kJ/mol, respectively (Figure S12 in the SI). For high precursor activation energy (E_A = 90 kJ/mol), the time scale of the temperature rise is much shorter compared to that of the monomer release rate, leading to a low concentration of bulk monomers during the temperature rise. Hence, the growth of nuclei into larger NPs is hindered. Since the rate of the temperature rise does not effectively change the monomer release rate (see eq 1), the dynamics of the system is approximately the same for all heating rates. For the low activation energy (E_A = 5 kJ/mol), the precursors are rapidly converted into the monomers, irrespective of the heating rate, leading to a rapid rise in the supersaturation, while the temperature of the system is not significantly changed.
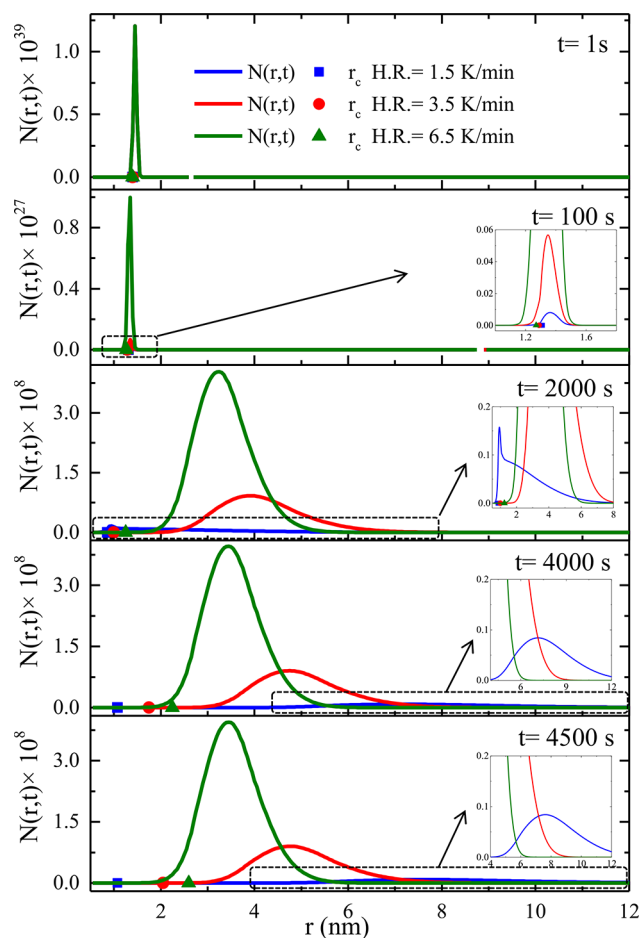

Figure 5. Simulated size distribution of nanoparticles at different simulation times: t = (a) 1, (b) 100, (c) 2000, (d) 4000, and (e) 4500 s. The precursor activation energy is E_A = 70 kJ/mol. In each panel, there are size distributions of the heating rates 1.5 (blue), 3.5 (red), and 6.5 (green) K/min; the critical radii are represented with blue■, red ●, and green ▲. The insets show an enlarged view of the marked region of the curves.

Therefore, the same nucleation rate is obtained for all heating rates, and the subsequent temperature rise with different rates does not remarkably change the growth dynamics of the nascent nuclei and the final NP size. The slightly larger NP size obtained for the case of lower activation energy compared to high activation energy is due to much higher supersaturation.

Size-Dependent Magnetic Properties. The hysteresis loops of the NPs at 300 and 2 K are shown in Figure 6a,b, respectively. At 300 K the A_1−A_6 NPs are superparamagnetic, whereas at 2 K particles show ferrimagnetic behavior.

The values of the saturation magnetization (M_s) of samples A_1−A_6 at room temperature and 2 K are plotted in Figure 6c as a function of inverse diameter. As the size of the NPs increases from 6.3 to 16.2 nm, M_s increases at 300 K from 54.8 to 79 emu/g and at 2 K from 64.1 to 85.7 emu/g. The M_s values are close to the reported values of 84 emu/g for pure bulk magnetite at 300 K.[51,52,20,53] The reduction in M_s with decreasing size can be explained by the existence of a surface spin disorder layer on the surface of the NPs, which is formed because of the lack of some oxygen ions from the spinel lattice, weak coordination of surface atoms, and the capping of the NPs with surfactants.[54−56] The thickness of the magnetically
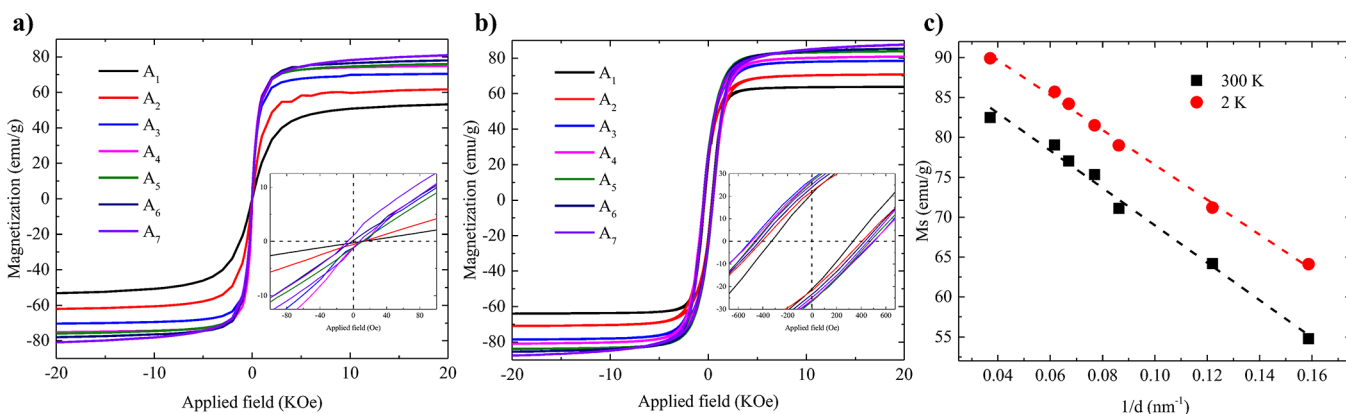
Figure 6. Hysteresis lopes of all samples at (a) 300 and (b) 2 K. (c) Saturation magnetization (M_s) versus the average diameter ($1/d$) of the NPs.
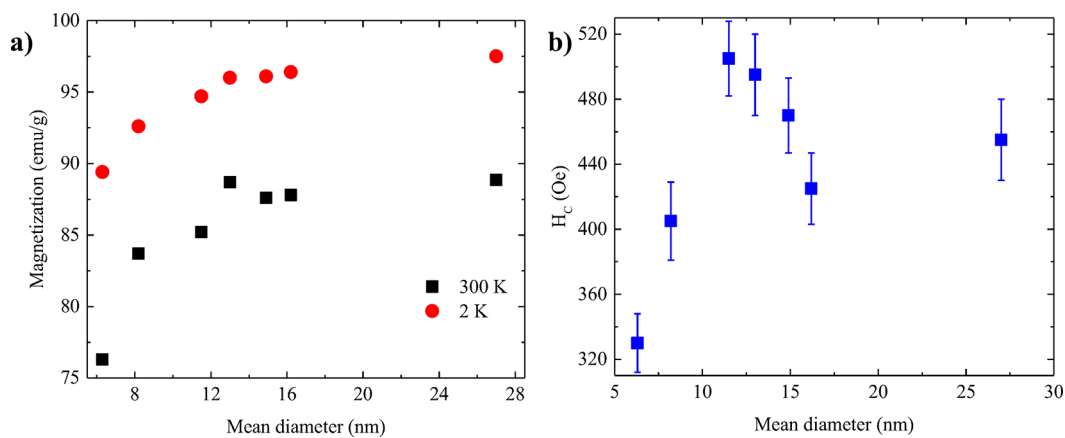

Figure 7. (a) Saturation magnetization of the sample after removing the mass of surfactant at 300 and 2 K. (b) Values of H_c as a function of size.
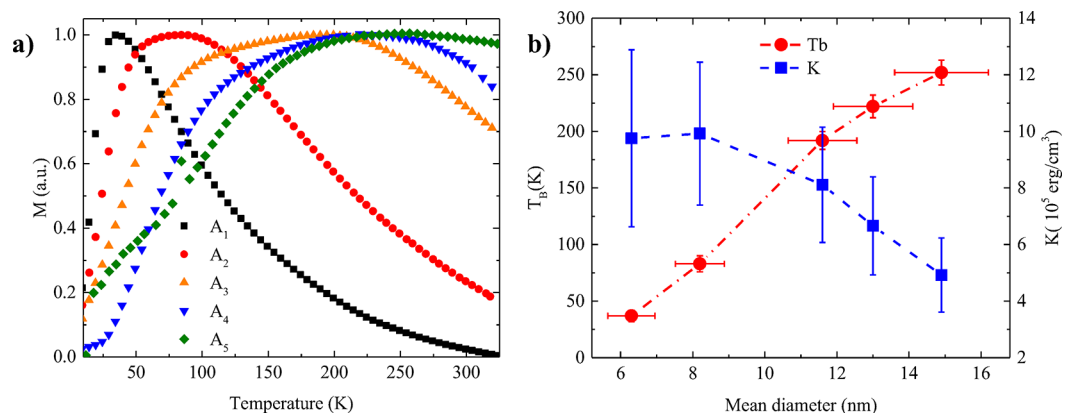

Figure 8. (a) Representative $M_{ZFC}-M_{FC}$ curves as a function of temperature for samples A_1-A_5. (b) Size dependence of T_B and K obtained from the ZFC−FC curve.

disordered shell can be calculated using the following relation:[54]

$$M_s = M_{s,(bulk)}\left(1 - \frac{6e}{d}\right) \qquad (3)$$

where e is thickness of the disordered layer, and d is the particle diameter. Using least-squares fitting, $M_{s,(bulk)}$ values of 92.4 and 98.4 emu/g at 300 and 2 K were obtained, respectively. The values of $M_{s,(bulk)}$ at 2 K are remarkably close to the theoretical value of 98 emu/g for Fe_3O_4.[57,58,52] The thickness of the spin-disordered layer was estimated using the values of $M_{s,(bulk)}$, and

amounted to 0.42 and 0.35 nm at 300 and 2 K, respectively (in agreement with previous reports).[54,59,60,23] The measured saturation magnetization was obtained for NPs covered with an organic surfactant. The saturated magnetization can be corrected by using only the mass of the iron oxide NPs obtained by TGA (Figure S7a). Corrected M_s values for different NPs do not show a strong dependence on the size for NPs larger than 8 nm, as shown in Figure 7a. Low-temperature M_s values approach the theoretical bulk value for pure single-crystalline magnetite (98 emu/g)[58,52] indicating size-independent, bulklike magnetic properties.[61,62] With an increase in the size of the NPs, the coercive field (H_c) raises up to the size of

11.6 nm, and then, with a further increase in the size, H_c decreases slightly as shown in Figure 7b. The behavior can be explained by the shifting of NPs from the single-domain to the multidomain regime.[25,7,63] The flipping of magnetic moments in each domain is controlled by magnetic anisotropy energy, domain wall motion, and thermal energy. When a NP is in the regime of a single domain, domain wall motion does not exist, and with an increase in the size of the magnetic anisotropy, the energy increases. As a result, H_c becomes higher. However, with a further increase in the size, the domains will be shifted to the multidomain regime, and because of the existence of domain wall motions, the coercivity becomes lower.

The magnetic anisotropy constant was determined via zero-field-cooling, and field-cooling (ZFC−FC) measurements. Upon increasing the temperature from 5 to 300 K, at blocking temperature, T_B, the thermal energy overcomes the magnetic anisotropy energy,[63,53] and the transition from ferro-ferrimagnetic to superparamagnetic takes place. A representative measurement at an applied magnetic field of 100 Oe for all the samples is given in Figure 8a. Evolution of T_B as a function of size is shown in Figure 8b. Upon decreasing size from 14.9 to 6.3 nm, the value of T_B is shifted to lower temperatures, in agreement with previous reports.[25,54,19] The magnetic anisotropy constant, K, was determined using following equation:[54,19]

$$K = \frac{25 k_B T_B}{V} \tag{4}$$

where k_B is Boltzmann's constant, and V is the volume of a single NP determined by TEM. The values of K, shown in Figure 8b, show an increase with decreasing particle size. The disorder of the NP's surface results in broken spin symmetry, i.e., surface anisotropy.[22,55,56] Therefore, the NPs with smaller sizes have a higher surface-to-volume ratio (higher surface anisotropy) and, as a result, a higher anisotropy constant and lower magnetization.

CONCLUSION

We have presented a combined experimental and theoretical study on the size evolution of iron oxide NPs by varying only the heating rate during synthesis. Superparamagnetic highly crystalline NPs with controllable size from 6 to 27 nm were obtained with a narrow size distribution typically below 10%. NPs showed nearly ideal magnetization values, which evolved with their size. Numerical simulations of nucleation and growth provided a valuable insight into the formation of the Fe_3O_4 NPs at different heating rates. The model reproduced the experimental trends, and showed that the relative time scales associated with the heating and precursor-to-monomer conversion rates is a decisive factor influencing the NP final size in thermal decomposition synthesis processes. For slow heating rates, large NPs with high polydispersity are predicted and obtained.

ASSOCIATED CONTENT

Ⓢ Supporting Information

The Supporting Information is available free of charge on the ACS Publications website at DOI: 10.1021/acs.chemmater.7b02872.

Experimental procedure; characterization of the nanoparticle with HRTEM, FTIR, TGA, and XRD; size distribution; effect of decomposition heating rate on the size and dispersity; calculated values of surfactant grafting density; and detailed discussion on the simulation procedure (PDF)

AUTHOR INFORMATION

Corresponding Authors
*E-mail: potestio@mpip-mainz.mpg.de.
*E-mail: asadi@mpip-mainz.mpg.de.

ORCID
Maziar Heidari: 0000-0002-8081-6602
Wolfgang Tremel: 0000-0002-4536-994X
Gerhard Jakob: 0000-0001-9466-0840
Davide Donadio: 0000-0002-2150-4182
Kamal Asadi: 0000-0003-0447-4337

Author Contributions
H.S.D. and A.H.R. performed the synthesis and subsequent size analysis and magnetic measurements. M.H., R.P., and D.D. performed the simulation. K.A. designed and supervised the work. The manuscript was written through contributions of all authors. All authors have given approval to the final version of the manuscript.

Notes
The authors declare no competing financial interest.

REFERENCES

(1) Dai, Q.; Berman, D.; Virwani, K.; Frommer, J.; Jubert, P.-O.; Lam, M.; Topuria, T.; Imaino, W.; Nelson, A. Self-assembled ferrimagnet polymer composites for magnetic recording media. *Nano Lett.* 2010, 10, 3216−3221.

(2) Yu, Y.; Mendoza-Garcia, A.; Ning, B.; Sun, S. Cobalt-substituted magnetite nanoparticles and their assembly into ferrimagnetic nanoparticle arrays. *Adv. Mater.* 2013, 25, 3090−3094.

(3) Sahoo, B.; Sahu, S. K.; Nayak, S.; Dhara, D.; Pramanik, P. Fabrication of magnetic mesoporous manganese ferrite nanocomposites as efficient catalyst for degradation of dye pollutants. *Catal. Sci. Technol.* 2012, 2, 1367−1374.

(4) De, M.; Ghosh, P. S.; Rotello, V. M. Applications of nanoparticles in biology. *Adv. Mater.* 2008, 20, 4225−4241.

(5) Frey, N. A.; Peng, S.; Cheng, K.; Sun, S. Magnetic nanoparticles: synthesis, functionalization, and applications in bioimaging and magnetic energy storage. *Chem. Soc. Rev.* 2009, 38, 2532−2542.

(6) Kim, J.; Piao, Y.; Hyeon, T. Multifunctional nanostructured materials for multimodal imaging, and simultaneous imaging and therapy. *Chem. Soc. Rev.* 2009, 38, 372−390.

(7) Kolhatkar, A. G.; Jamison, A. C.; Litvinov, D.; Willson, R. C.; Lee, T. R. Tuning the magnetic properties of nanoparticles. *Int. J. Mol. Sci.* 2013, 14, 15977−16009.

(8) Mohapatra, J.; Mitra, A.; Bahadur, D.; Aslam, M. Surface controlled synthesis of MFe_2O_4 (M= Mn, Fe, Co, Ni and Zn)

nanoparticles and their magnetic characteristics. *CrystEngComm* **2013**, *15*, 524−532.

(9) Yang, C.; Wu, J.; Hou, Y. Fe$_3$O$_4$ nanostructures: synthesis, growth mechanism, properties and applications. *Chem. Commun.* **2011**, *47*, 5130−5141.

(10) Demortiere, A.; Panissod, P.; Pichon, B.; Pourroy, G.; Guillon, D.; Donnio, B.; Begin-Colin, S. Size-dependent properties of magnetic iron oxide nanocrystals. *Nanoscale* **2011**, *3*, 225−232.

(11) Park, J.; Lee, E.; Hwang, N. M.; Kang, M.; Kim, S. C.; Hwang, Y.; Park, J. G.; Noh, H. J.; Kim, J. Y.; Park, J. H. One-nanometer-scale size-controlled synthesis of monodisperse magnetic Iron oxide nanoparticles. *Angew. Chem.* **2005**, *117*, 2932−2937.

(12) Ahn, T.; Kim, J. H.; Yang, H.-M.; Lee, J. W.; Kim, J.-D. Formation pathways of magnetite nanoparticles by coprecipitation method. *J. Phys. Chem. C* **2012**, *116*, 6069−6076.

(13) Cai, W.; Wan, J. Facile synthesis of superparamagnetic magnetite nanoparticles in liquid polyols. *J. Colloid Interface Sci.* **2007**, *305*, 366−370.

(14) Daou, T.; Pourroy, G.; Begin-Colin, S.; Greneche, J.; Ulhaq-Bouillet, C.; Legaré, P.; Bernhardt, P.; Leuvrey, C.; Rogez, G. Hydrothermal synthesis of monodisperse magnetite nanoparticles. *Chem. Mater.* **2006**, *18*, 4399−4404.

(15) Lee, Y.; Lee, J.; Bae, C. J.; Park, J. G.; Noh, H. J.; Park, J. H.; Hyeon, T. Large-scale synthesis of uniform and crystalline magnetite nanoparticles using reverse micelles as nanoreactors under reflux conditions. *Adv. Funct. Mater.* **2005**, *15*, 503−509.

(16) Tang, N.; Zhong, W.; Jiang, H.; Wu, X.; Liu, W.; Du, Y. Nanostructured magnetite (Fe$_3$O$_4$) thin films prepared by sol−gel method. *J. Magn. Magn. Mater.* **2004**, *282*, 92−95.

(17) Guardia, P.; Pérez, N.; Labarta, A.; Batlle, X. Controlled synthesis of iron oxide nanoparticles over a wide size range. *Langmuir* **2010**, *26*, 5843−5847.

(18) Kovalenko, M. V.; Bodnarchuk, M. I.; Lechner, R. T.; Hesser, G.; Schäffler, F.; Heiss, W. Fatty acid salts as stabilizers in size-and shape-controlled nanocrystal synthesis: the case of inverse spinel iron oxide. *J. Am. Chem. Soc.* **2007**, *129*, 6352−6353.

(19) Park, J.; An, K.; Hwang, Y.; Park, J.-G.; Noh, H.-J.; Kim, J.-Y.; Park, J.-H.; Hwang, N.-M.; Hyeon, T. Ultra-large scale syntheses of monodisperse nanocrystals. *Nat. Mater.* **2004**, *3*, 891−895.

(20) Sun, S.; Zeng, H.; Robinson, D. B.; Raoux, S.; Rice, P. M.; Wang, S. X.; Li, G. Monodisperse MFe$_2$O$_4$ (M= Fe, Co, Mn) nanoparticles. *J. Am. Chem. Soc.* **2004**, *126*, 273−279.

(21) Sun, S.; Zeng, H. Size-controlled synthesis of magnetite nanoparticles. *J. Am. Chem. Soc.* **2002**, *124*, 8204−8205.

(22) Huang, J.-H.; Parab, H. J.; Liu, R.-S.; Lai, T.-C.; Hsiao, M.; Chen, C.-H.; Sheu, H.-S.; Chen, J.-M.; Tsai, D.-P.; Hwu, Y.-K. Investigation of the growth mechanism of iron oxide nanoparticles via a seed-mediated method and its cytotoxicity studies. *J. Phys. Chem. C* **2008**, *112*, 15684−15690.

(23) Zheng, M.; Wu, X.; Zou, B.; Wang, Y. Magnetic properties of nanosized MnFe$_2$O$_4$ particles. *J. Magn. Magn. Mater.* **1998**, *183*, 152−156.

(24) Meledandri, C. J.; Stolarczyk, J. K.; Ghosh, S.; Brougham, D. F. Nonaqueous magnetic nanoparticle suspensions with controlled particle size and nuclear magnetic resonance properties. *Langmuir* **2008**, *24*, 14159−14165.

(25) Baaziz, W.; Pichon, B. P.; Fleutot, S.; Liu, Y.; Lefevre, C.; Greneche, J.-M.; Toumi, M.; Mhiri, T.; Begin-Colin, S. Magnetic iron oxide nanoparticles: reproducible tuning of the size and nanosized-dependent composition, defects, and spin canting. *J. Phys. Chem. C* **2014**, *118*, 3795−3810.

(26) Bronstein, L. M.; Huang, X.; Retrum, J.; Schmucker, A.; Pink, M.; Stein, B. D.; Dragnea, B. Influence of iron oleate complex structure on iron oxide nanoparticle formation. *Chem. Mater.* **2007**, *19*, 3624−3632.

(27) Hyeon, T.; Lee, S. S.; Park, J.; Chung, Y.; Na, H. B. Synthesis of highly crystalline and monodisperse maghemite nanocrystallites without a size-selection process. *J. Am. Chem. Soc.* **2001**, *123*, 12798−12801.

(28) Van Embden, J.; Chesman, A. S.; Jasieniak, J. J. The heat-up synthesis of colloidal nanocrystals. *Chem. Mater.* **2015**, *27*, 2246−2285.

(29) Van Embden, J.; Sader, J. E.; Davidson, M.; Mulvaney, P. Evolution of colloidal nanocrystals: theory and modeling of their nucleation and growth. *J. Phys. Chem. C* **2009**, *113*, 16342−16355.

(30) LaMer, V. K.; Dinegar, R. H. Theory, production and mechanism of formation of monodispersed hydrosols. *J. Am. Chem. Soc.* **1950**, *72*, 4847−4854.

(31) Kwon, S. G.; Piao, Y.; Park, J.; Angappane, S.; Jo, Y.; Hwang, N.-M.; Park, J.-G.; Hyeon, T. Kinetics of monodisperse iron oxide nanocrystal formation by "heating-up" process. *J. Am. Chem. Soc.* **2007**, *129*, 12571−12584.

(32) Park, J.; Joo, J.; Kwon, S. G.; Jang, Y.; Hyeon, T. Synthesis of monodisperse spherical nanocrystals. *Angew. Chem., Int. Ed.* **2007**, *46*, 4630−4660.

(33) Talapin, D. V.; Rogach, A. L.; Haase, M.; Weller, H. Evolution of an ensemble of nanoparticles in a colloidal solution: theoretical study. *J. Phys. Chem. B* **2001**, *105*, 12278−12285.

(34) Van Embden, J.; Mulvaney, P. Nucleation and growth of CdSe nanocrystals in a binary ligand system. *Langmuir* **2005**, *21*, 10226−10233.

(35) Wu, L.; Jubert, P.-O.; Berman, D.; Imaino, W.; Nelson, A.; Zhu, H.; Zhang, S.; Sun, S. Monolayer Assembly of Ferrimagnetic Co$_x$Fe$_{3−x}$O$_4$ Nanocubes for Magnetic Recording. *Nano Lett.* **2014**, *14*, 3395−3399.

(36) Abbas, M.; Torati, S. R.; Kim, C. A novel approach for the synthesis of ultrathin silica-coated iron oxide nanocubes decorated with silver nanodots (Fe$_3$O$_4$/SiO$_2$/Ag) and their superior catalytic reduction of 4-nitroaniline. *Nanoscale* **2015**, *7*, 12192−12204.

(37) Eom, Y.; Abbas, M.; Noh, H.; Kim, C. Morphology-controlled synthesis of highly crystalline Fe$_3$O$_4$ and CoFe$_2$O$_4$ nanoparticles using a facile thermal decomposition method. *RSC Adv.* **2016**, *6*, 15861−15867.

(38) Klug, H. P.; Alexander, L. E. *X-ray diffraction procedures*; Wiley: New York, 1954.

(39) Miguel-Sancho, N.; Bomati-Miguel, O.; Roca, A. G.; Martinez, G.; Arruebo, M.; Santamaria, J. Synthesis of magnetic nanocrystals by thermal decomposition in glycol media: effect of process variables and mechanistic study. *Ind. Eng. Chem. Res.* **2012**, *51*, 8348−8357.

(40) Belaïd, S.; Laurent, S.; Vermeersch, M.; Vander Elst, L.; Perez-Morga, D.; Muller, R. N. A new approach to follow the formation of iron oxide nanoparticles synthesized by thermal decomposition. *Nanotechnology* **2013**, *24*, 055705−055713.

(41) Cornell, R. M.; Schwertmann, U. *The iron oxides: structure, properties, reactions, occurrences and uses*; John Wiley & Sons: New York, 2003.

(42) Pascu, O.; Carenza, E.; Gich, M.; Estradé, S. n.; Peiró, F.; Herranz, G.; Roig, A. Surface reactivity of iron oxide nanoparticles by microwave-assisted synthesis; comparison with the thermal decomposition route. *J. Phys. Chem. C* **2012**, *116*, 15108−15116.

(43) Lynch, J.; Zhuang, J.; Wang, T.; LaMontagne, D.; Wu, H.; Cao, Y. C. Gas-bubble effects on the formation of colloidal iron oxide nanocrystals. *J. Am. Chem. Soc.* **2011**, *133*, 12664−12674.

(44) Perala, S. R. K.; Kumar, S. On the two-step mechanism for synthesis of transition-metal nanoparticles. *Langmuir* **2014**, *30*, 12703−12711.

(45) Rempel, J. Y.; Bawendi, M. G.; Jensen, K. F. Insights into the kinetics of semiconductor nanocrystal nucleation and growth. *J. Am. Chem. Soc.* **2009**, *131*, 4479−4489.

(46) Rinaldo, S. G.; Lee, W.; Stumper, J.; Eikerling, M. Non-monotonic dynamics in Lifshitz-Slyozov-Wagner theory: Ostwald ripening in nanoparticle catalysts. *Phys. Rev. E* **2012**, *86*, 041601−041610.

(47) Singh, A.; Puri, S.; Dasgupta, C. Growth kinetics of nanoclusters in solution. *J. Phys. Chem. B* **2012**, *116*, 4519−4523.

(48) Voss, B.; Haase, M. Intrinsic focusing of the particle size distribution in colloids containing nanocrystals of two different crystal phases. *ACS Nano* **2013**, *7*, 11242−11254.

(49) Timonen, J. V.; Seppälä, E. T.; Ikkala, O.; Ras, R. H. From Hot-Injection Synthesis to Heating-Up Synthesis of Cobalt Nanoparticles: Observation of Kinetically Controllable Nucleation. *Angew. Chem., Int. Ed.* **2011**, *50*, 2080−2084.

(50) Muscas, G.; Singh, G.; Glomm, W.; Mathieu, R.; Kumar, P. A.; Concas, G.; Agostinelli, E.; Peddis, D. Tuning the size and shape of oxide nanoparticles by controlling oxygen content in the reaction environment: morphological analysis by aspect maps. *Chem. Mater.* **2015**, *27*, 1982−1990.

(51) O'grady, K.; Bradbury, A. Particle size analysis in ferrofluids. *J. Magn. Magn. Mater.* **1983**, *39*, 91−94.

(52) Roca, A. G.; Marco, J. F.; Morales, M. d. P.; Serna, C. J. Effect of nature and particle size on properties of uniform magnetite and maghemite nanoparticles. *J. Phys. Chem. C* **2007**, *111*, 18577−18584.

(53) Wu, L.; Mendoza-Garcia, A.; Li, Q.; Sun, S. Organic phase syntheses of magnetic nanoparticles and their applications. *Chem. Rev.* **2016**, *116*, 10473−10512.

(54) Caruntu, D.; Caruntu, G.; O'Connor, C. J. Magnetic properties of variable-sized Fe_3O_4 nanoparticles synthesized from non-aqueous homogeneous solutions of polyols. *J. Phys. D: Appl. Phys.* **2007**, *40*, 5801−5809.

(55) Kodama, R.; Berkowitz, A.; McNiff, E., Jr; Foner, S. Surface spin disorder in ferrite nanoparticles. *J. Appl. Phys.* **1997**, *81*, 5552−5557.

(56) Morales, M. d. P.; Veintemillas-Verdaguer, S.; Montero, M.; Serna, C.; Roig, A.; Casas, L.; Martinez, B.; Sandiumenge, F. Surface and internal spin canting in γ-Fe_2O_3 nanoparticles. *Chem. Mater.* **1999**, *11*, 3058−3064.

(57) Guardia, P.; Labarta, A.; Batlle, X. Tuning the size, the shape, and the magnetic properties of iron oxide nanoparticles. *J. Phys. Chem. C* **2011**, *115*, 390−396.

(58) Roca, A.; Morales, M.; O'Grady, K.; Serna, C. Structural and magnetic properties of uniform magnetite nanoparticles prepared by high temperature decomposition of organic precursors. *Nanotechnology* **2006**, *17*, 2783−2788.

(59) Chen, J.; Sorensen, C.; Klabunde, K.; Hadjipanayis, G.; Devlin, E.; Kostikas, A. Size-dependent magnetic properties of $MnFe_2O_4$ fine particles synthesized by coprecipitation. *Phys. Rev. B: Condens. Matter Mater. Phys.* **1996**, *54*, 9288−9296.

(60) Liu, C.; Zhang, Z. J. Size-dependent superparamagnetic properties of Mn spinel ferrite nanoparticles synthesized from reverse micelles. *Chem. Mater.* **2001**, *13*, 2092−2096.

(61) Guardia, P.; Perez-Juste, J.; Labarta, A.; Batlle, X.; Liz-Marzán, L. M. Heating rate influence on the synthesis of iron oxide nanoparticles: the case of decanoic acid. *Chem. Commun.* **2010**, *46*, 6108−6110.

(62) Perez, N.; Guardia, P.; Roca, A. G.; Morales, M. d. P.; Serna, C. J.; Iglesias, O.; Bartolome, F.; Garcia, L. M.; Batlle, X.; Labarta, A. Surface anisotropy broadening of the energy barrier distribution in magnetic nanoparticles. *Nanotechnology* **2008**, *19*, 475704−475711.

(63) Leslie-Pelecky, D. L.; Rieke, R. D. Magnetic properties of nanostructured materials. *Chem. Mater.* **1996**, *8*, 1770−1783.